ROYAL SOCIETY OF CHEMISTRY

PAPER

Check for updates

Ultrasmall Mn-doped iron oxide nanoparticles with dual hepatobiliary and renal clearances for T_1 MR liver imaging†

Sanghoon Lee,[a] Arim Byun,[a] Juhee Jo,[b] Jong-Min Suh, [c] Jeasang Yoo, [c] Mi Hee Lim, [c] Ji-wook Kim, [*b] Tae-Hyun Shin [*b] and Jin-sil Choi [*a]

Although magnetic nanoparticles demonstrate significant potential as magnetic resonance imaging (MRI) contrast agents, their negative contrasts, liver accumulation, and limited excretion hinder their application. Herein, we developed ultrasmall Mn-doped iron oxide nanoparticles (UMIOs) with distinct advantages as T_1 MRI contrast agents. Exceptionally small particle sizes (*ca.* 2 nm) and magnetization values (5 emu g_{Mn+Fe}^{-1}) of UMIOs provided optimal T_1 contrast effects with an ideally low r_2/r_1 value of ~1. Furthermore, the use of Mn as a dopant facilitated hepatocyte uptake of the particles, allowing liver imaging. In animal studies, UMIOs exhibited significantly enhanced contrasts for sequential T_1 imaging of blood vessels and the liver, distinguishing them from conventional magnetic nanoparticles. UMIOs were systematically cleared *via* dual hepatobiliary and renal excretion pathways, highlighting their safety profile. These characteristics imply substantial potential of UMIOs as T_1 contrast agents for the accurate diagnosis of liver diseases.

Introduction

Magnetic resonance imaging (MRI) is one of the powerful diagnostic modalities widely used for the diagnosis of liver diseases.[1] It provides superior contrast between different tissues/lesions and offers outstanding safety as compared to other imaging techniques such as computed tomography and X-ray.[2] In the context of liver tumor diagnosis, it is crucial to visualize not only the liver, but also its vascular structures.[3,4] The development of liver-specific gadolinium (Gd)-based contrast agents (GBCAs), such as gadoxetate disodium (Gd-EOB-DTPA), has greatly enhanced the utility of MRI in hepato-cellular carcinoma (HCC) diagnosis.[3,4] When Gd-EOB-DTPA is intravenously administered, it exhibits a positive (T_1) contrast effect in blood vessels, allowing the imaging of tumor associated vasculatures.[5] Subsequently, it is taken up by hepatocytes *via* organic anion transporter polypeptide (OATP) receptors for liver imaging.[6,7] Since cancerized hepatic cells weakly express

OATP receptors and do not take up Gd-EOB-DTPA, no contrast enhancement is observed in the region affected by HCC. This lack of enhancement aids in the diagnosis of HCC.[8] However, the currently available hepatocyte-specific GBCA, Gd-EOB-DTPA, has limitations in terms of sensitivity and specificity, especially in detecting small tumors or those with abnormal expression of OATP receptors. Furthermore, it raises safety related concerns as it is based on a toxic Gd ion, which can induce a potentially fatal fibrosing disease affecting multiple organs[9,10] and has been associated with various side effects, including unexplained breathing difficulties.[11,12]

Superparamagnetic iron oxide nanoparticles (SPIOs), such as Feridex® and Resovist®, are representative Gd-free T_2 (negative) MRI contrast agents used for liver imaging.[13,14] They have been utilized for liver imaging due to their biocompatibilities and biodegradabilities.[15] Unlike Gd-EOB-DTPA, SPIOs enter the liver *via* the monophagocytic system (for example, Kupffer cells).[16,17] Due to the relatively low densities of Kupffer cells in HCC lesions, the nanoparticle population and resulting signal intensity are lower in these lesions compared to normal liver tissue. While SPIOs offer an effective alternative route for liver imaging, their negative T_2 contrast effects hinder vascular imaging.[18] Additionally, once taken up by Kupffer cells, SPIOs are retained in the human body for a long period of time.

To address these limitations, previous studies have explored ultrasmall superparamagnetic iron oxide nanoparticles (USPIOs) with the aim of achieving T_1 (positive) contrast effects and visualization of blood vessels.[19–26] However, the successful demonstration of USPIOs that simultaneously provide

aDepartment of Chemical and Biological Engineering, Hanbat National University, Daejeon 34158, Korea. E-mail: jisil.choi@hanbat.ac.kr

bInventera Inc., Seoul 06588, Republic of Korea. E-mail: thshin@inventerapharm.com; jwkim@inventerapharm.com

cDepartment of Chemistry, Korea Advanced Institute of Science and Technology (KAIST), Daejeon 34141, Korea

appropriate contrast effects for both blood vessels and the liver is challenging.[27] Notably, USPIOs lose their T_1 contrast effects after uptake by Kupffer cells, possibly owing to aggregation and increased magnetization within intracellular environments, due to their limited colloidal stabilities.[28]

In this study, we report ultrasmall Mn-doped iron oxide nanoparticles (UMIOs) with an ultrasmall size of approximately 2 nm. UMIO was obtained through the coprecipitation method, which has various advantages in terms of economic aspects compared to other synthetic methods. These nanoparticles demonstrate sequential T_1 imaging of blood vessels and the liver, underscoring their potential as liver contrast agents. The significant feature of UMIOs is their substantially low magnetization values, comparable to that of typical GBCA, which allow UMIOs to exhibit optimal T_1 contrast effects with ideally low r_2/r_1 values.[29] Moreover, because of their exceptional colloidal stabilities, UMIOs maintain T_1 contrast effects in blood vessels and show strong T_1 signals even after liver uptake.[30] An additional advantage of UMIOs is their specific entry into the liver *via* solute carrier family 39 member 14 (SLC39A14, a transmembrane metal transporter) mediated hepatocyte uptake facilitated by doping of manganese ions,[31,32] unlike other SPIO based contrast agents, which are taken up by Kupffer cells.[18] Furthermore, UMIOs, which are designed based on biocompatible iron oxide,[33–35] are cleared in the liver *via* the hepatobiliary pathway, and the remaining portion of UMIOs that does not enter the liver is eliminated *via* renal clearance ensuring their safety.

Experimental section

Reagents

All reagents were used without purification. Iron(III) chloride hexahydrate (FeCl$_3$·6H$_2$O, 97%, Sigma-Aldrich), iron(II) chloride tetrahydrate (FeCl$_2$·4H$_2$O, ≥99%, Sigma-Aldrich), manganese(II) chloride tetrahydrate (MnCl$_2$·4H$_2$O, ≥98%, Daejung), hydrochloric acid (HCl, 35–37%, Samchun), ammonia solution (NH$_4$OH, 28–30%, Samchun), polyacrylic acid (PAA, MW: 2000, 63 wt% aqueous solution, Acros Organics), sodium hydroxide (NaOH, 93%, Duksan), sodium citrate dihydrate (Na$_3$C$_6$H$_5$O$_7$·2H$_2$O, ≥99%, Daejung), citric acid (C$_6$H$_8$O$_7$, 99.5%, Samchun), sodium phosphate dibasic (Na$_2$HPO$_4$, 99%, Samchun), sodium phosphate monobasic dihydrate (NaH$_2$PO$_4$·2H$_2$O, 98–102%, Samchun), sodium carbonate (Na$_2$CO$_3$, 99%, Samchun), sodium bicarbonate (NaHCO$_3$, 99–100.5%, Samchun), fetal bovine serum (FBS, Merck Millipore), Dulbecco's modified eagle medium (DMEM, Welgene), penicillin–streptomycin (Pen–Strep, Gibco), saline (0.9% NaCl, JW Life Science), cell counting kit-8 (CCK-8, Sigma-Aldrich), and phosphate buffered saline (PBS, pH = 7.4, 10 mM, Sigma-Aldrich) were used.

Equipment

Shapes and sizes of UMIOs were analyzed using field-emission transmission electron microscopy (TEM, Tecnai G^2 F30 S-TWIN, FEI, Netherlands). The contents of Mn and Fe and crystalline structures of UMIOs were investigated by X-ray photoelectron spectroscopy (XPS, K-Alpha+, Thermo Fisher Scientific, USA), energy-dispersive X-ray spectroscopy (EDS, HF5000, Hitachi, Japan), and X-ray diffraction (XRD, SmartLab, Rigaku, Japan). The chemical functional groups and composition of UMIOs were examined through Fourier-transform infrared spectrometry (FT-IR, Nicolet 6700, Thermo Fisher Scientific, USA). Hydrodynamic diameters of UMIOs in an aqueous solution were measured using Zetasizer (ZSU3200, Malvern Panalytical, England), and magnetic properties of these nanoparticles were examined using X-band electron paramagnetic resonance spectroscopy (EPR, Bruker BioSpin, Silberstreifen, Rheinstetten, Germany) and a superconducting quantum interference device-vibrating sample magnetometer (SQUID-VSM, QM02, Quantum Design, USA). In toxicity experiments, the absorbance was evaluated using a multi-mode microplate reader (SpectraMax M2, Molecular Devices, USA).

Synthesis of ultrasmall Mn-doped iron oxide nanoparticles (UMIOs)

UMIOs were synthesized *via* a modified coprecipitation method.[36–41] Typically, PAA (4.56 mmol) was mixed with 25 mL distilled water as the solvent. Then, the mixture was bubbled with Ar gas for 40 min followed by heating to 65 °C. To prepare an Fe/Mn solution, FeCl$_3$·6H$_2$O (0.0717 mmol) and MnCl$_2$·4H$_2$O (0.142 mmol) were dissolved in 1 mL HCl (1 M). Thereafter, the Fe and Mn salt solution was injected into the PAA solution while maintaining a temperature of 65 °C. Then, 3.5 mL NH$_4$OH was introduced into the resulting solution, and the reaction was performed at 65 °C for 2 h. The resulting solution was purified three times by centrifugation with acetone and five times with an ultrafiltration (Amicon, molecular cutoff: 10 K, Millipore) to acquire UMIOs.

Magnetic resonance imaging (MRI)

A 3 Tesla (T) preclinical MRI system (MRS 3000 series, MR solution) was utilized for phantom imaging, r_1 and r_2 measurements, and blood vessel and liver MRI. The related specification and sequences were as follows: clear-bore size: 17 cm; gradient strength: 600 mT m^{-1}; radiofrequency amplifier power: 500 W; radiofrequency coil diameter of 35 mm and length of 140 mm; operating software: Preclinical Scan. T_1 scans were conducted using a coronal fast low-angle shot (FLASH) sequence with the following parameters: TE: 3.8 ms; TR: 13 ms; FA: 20°; FOV: 60 × 30 × 16 mm^3; matrix size: 256 × 72 × 16; resolution 0.23 × 0.42 × 1 mm^3. A total of ten image series (each consisting of 16 coronal slices) were scanned after the intravenous injection of contrast agents. The first five series were acquired with a time interval of 2 min, and the subsequent five series were acquired with a time interval of 10 minutes. The acquisition time for each image series was 15 seconds. For the T_2 scan, the MR parameters were as follows: TE: 34 ms; TR: 4500 ms; echo train length: 4; FOV: 60 × 30 × 16 mm^3; resolution: 0.23 × 0.23 × 1 mm^3; and slice orientation: coronal. r_1 and r_2 values were calculated according to the literature.[42]

A 9.4 T preclinical MRI system (BioSpec 94/20 USR, Bruker BioSpin) was utilized for excretion studies, and the

corresponding specifications were as follows: TR: 7.5 ms; TE: 2.349 ms; matrix size: $256 \times 96 \times 36$; resolution: 0.312 mm per pixel $\times$ 0.312 mm per pixel $\times$ 0.624 mm per pixel; FOV: 79.9 mm $\times$ 30 mm $\times$ 22.464 mm; slice thickness: 22.46 mm; scan time: 15 s and 120 ms; dimension: three-dimensional; coil: 72 mm; flip angle: 20 degree; and repetition: 1.

Animal injection

BALB/c mice (Orient Bio) were used for animal MRI studies. All experiments were performed in accordance with the protocols approved by the Institutional Animal Care and Use Committee of Yonsei University College of Medicine (approval number: 2023-0067). Mice were anesthetized with isoflurane (Hana Pharm Co., Ltd.) in oxygen before MR imaging. The contrast agent was administered intravenously. For animal toxicity studies, ICR mice (Samtako Bio Korea) were utilized. Body weight and clinical signs were monitored following the intravenous injection of the contrast agent. Animal toxicity study was carried out by QuBEST BIO, a contracted research organization

(study no. 0906222450) and all experiments were performed in accordance with protocols approved by the Institutional Animal Care and Use Committee of QuBEST BIO (approval number: QBIACUC-A22450).

Results and discussion

UMIOs were synthesized using a coprecipitation method, and their surfaces were stabilized with PAA, which is mixed during the reaction. In the FT-IR spectrum (Fig. S1†), coordination of PAA (–COOH) on the surface of iron oxide is confirmed.[43,44] The resulting nanoparticles were round-shaped with sizes of *ca.* 2.3 $\pm$ 0.5 nm (Fig. 1a) and had hydrodynamic sizes of *ca.* 3.9 $\pm$ 0.6 nm (Fig. 1b), which enabled their stable dispersion in aqueous solution. UMIOs exhibited a negative charge (-32.5 ± 1.81 mV) due to dense surface coating of PAA. The efficient coordination of UMIOs with the COOH groups of PAA is not only beneficial for maintaining their small size but also ensures solubility in aqueous solutions without requiring additional surface modification. EDX mapping images indicated that Fe
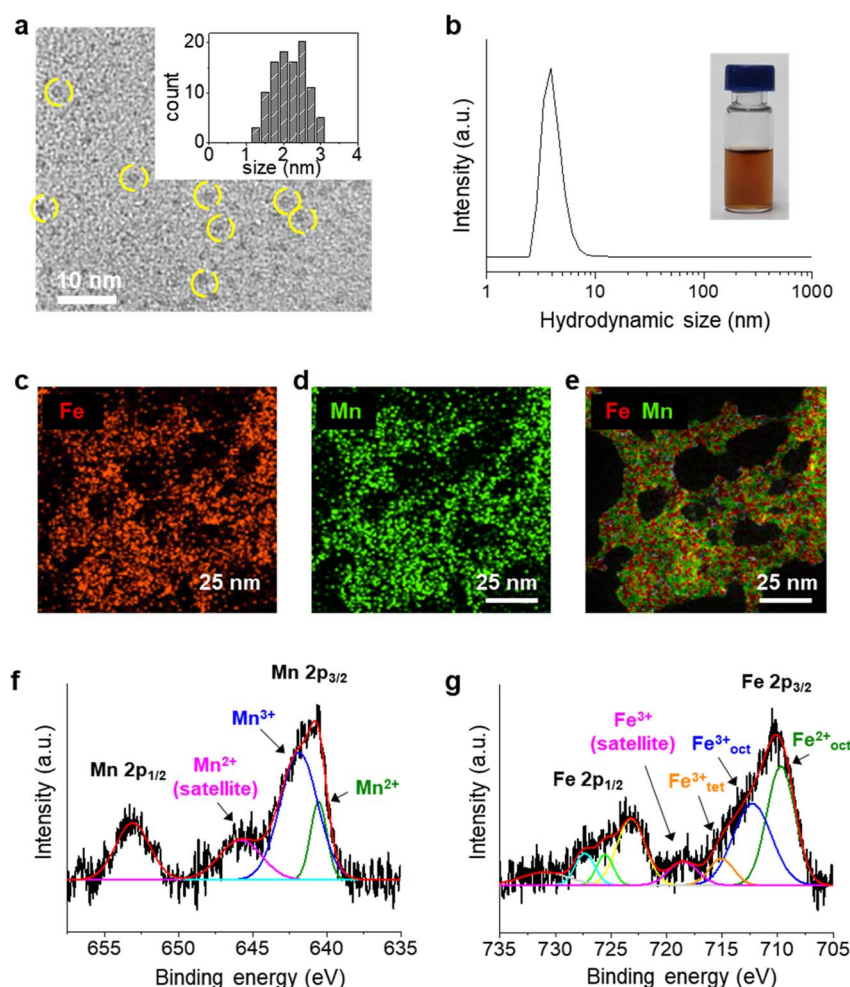

Fig. 1 Characterization of ultrasmall Mn-doped iron oxide nanoparticles (UMIOs). (a) Transmission electron microscope (TEM) image and size histogram (inset) of UMIOs. (b) Hydrodynamic sizes and image of UMIOs dispersed in aqueous solution. (c–e) Energy-dispersive X-ray spectroscopy (EDX) mapping images of Fe (c), Mn (d), and their overlap (e). (f and g) High-resolution X-ray photoelectron spectroscopy (XPS) spectra of Mn (f) and Fe (g) in UMIOs.

(Fig. 1c) and Mn (Fig. 1d) ions were evenly distributed throughout the nanoparticles with their locations perfectly overlapping (Fig. 1e).

Chemical states of Mn and Fe ions in UMIOs were determined using XPS (Fig. 1f and g). In the high-resolution XPS spectrum of Mn, two main peaks were observed at 641.2 (Mn $2p_{3/2}$) and 652.8 eV (Mn $2p_{1/2}$) along with a satellite peak at 644.9 eV (pink) that matched the peak of the Mn^{2+} chemical state.[45–48] The deconvoluted peaks of Mn $2p_{3/2}$ demonstrated that Mn existed in both its Mn^{2+} (640.5 eV, green) and Mn^{3+} (641.9 eV, blue) states.[47–49] The XPS spectrum of Fe exhibited two major peaks at 711.1 (Fe $2p_{3/2}$) and 725 eV (Fe $2p_{1/2}$), and the deconvoluted peaks of Fe $2p_{3/2}$ demonstrated that Fe existed in both its Fe^{2+} state (Fe_{oct}^{2+} peak: 709.7 eV (green)) and Fe^{3+} states (Fe_{oct}^{3+} peak: 712.3 eV (blue) and Fe_{tet}^{3+} peak: 715.1 eV (orange), and a satellite peak: 719.2 eV (pink)).[50–57] Fe^{2+} in UMIOs is formed by partial reduction of Fe^{3+} ions by ammonia and Mn ions.[58–60] The Fe : Mn ratio was measured to be approximately 0.6 : 0.4 by inductively coupled plasma optical emission spectroscopy (ICP-OES) and EDX mapping (Table S1†). However, XRD analyses of UMIOs exhibited no sharp peaks (Fig. S2†), likely attributable to their small size, even though crystal structures were observed in high resolution TEM images (Fig. S3†).

Magnetic properties of UMIOs were compared with those of USPIOs (2.74 nm, Fig. S4†) and Dotarem (a representative commercially available T_1 MRI contrast agent) by obtaining magnetization (M) curves of these materials at a sweeping field of $H = \pm 15$ kOe. UMIOs exhibited a paramagnetic M–H curve, which was similar to that of Dotarem, whereas USPIOs exhibited a superparamagnetic behavior (Fig. 2a). UMIOs demonstrated a very small magnetization value (5 emu g_{Mn+Fe}^{-1}, Fig. 2a) at 15 kOe, which was comparable to that of Dotarem (5 emu g_{Gd}^{-1}) and approximately 6 times smaller than that of USPIOs (32 emu g_{Fe}^{-1}). In addition, the EPR spectrum of UMIOs showed hyperfine splitting from Mn ions with a relatively low signal intensity compared to that of USPIOs (Fig. S5†).[61–63]

Moreover, the linewidth (ΔH_{pp}) of UMIOs (61.3 G) was broader than that of USPIOs (50.1 G), indicating a slower electron relaxation time.[64]

UMIOs exhibited brighter signals at all tested concentrations (Fig. 2b) as compared to those of USPIOs (Fig. 2c) and Dotarem (Fig. 2d) in T_1-weighted images acquired using a 3 T MRI scanner. The measured r_1 values of UMIOs, USPIOs, and Dotarem were 22.5, 8.8, and 3.9 mM^{-1} s^{-1}, respectively (Fig. 2e and S6†). UMIOs and USPIOs exhibited similar r_2 values of 25.0 and 22.5 mM^{-1} s^{-1}, respectively. However, Dotarem showed a relatively small r_2 value of 4.6 mM^{-1} s^{-1}. The r_2/r_1 ratio, a crucial parameter for evaluating the performances of T_1 MRI contrast agents, was 1.1 for UMIOs and 1.2 for Dotarem, whereas it was 2.6 for USPIOs (Fig. 2f). These excellent T_1 MRI contrast effects of UMIOs are attributed to their paramagnetic behaviors, which are achieved by their small particle sizes and Mn dopants.

Colloidal stabilities and safeties of UMIOs under physiological conditions are important factors for the biomedical applications of UMIOs. UMIOs were stably dispersed in saline and aqueous solutions over wide ranges of pH without significant changes in their hydrodynamic sizes (Fig. S7 and S8†). Moreover, UMIOs maintained consistent hydrodynamic sizes after being incubated in aqueous solutions with high protein contents (e.g., 5 and 10% fetal bovine serum), indicating their anti-opsonizing properties (Fig. S9†). In in vitro safety tests, UMIOs exhibited no considerable toxic effects on cells, including A549 (lung cancer cell line) and HepG2 (liver cancer cell line), even at concentrations up to 1250 μg$_{Fe+Mn}$ mL^{-1} (Fig. S10†). In the hemolysis assay of UMIOs in mouse whole blood, no significant hemolysis was observed at the estimated blood concentration of UMIOs at a dose level of up to 5.6 mg kg^{-1} (Fig. S11†). Furthermore, when tested in live animals, UMIOs showed no toxic effects following intravenous injection at dosages up to 15 mg$_{Fe+Mn}$ kg^{-1}, which was more than 5-fold the dose required for in vivo imaging (Fig. S12 and Table S2†). All these results imply that UMIOs possess outstanding biocompatibilities for biomedical applications.
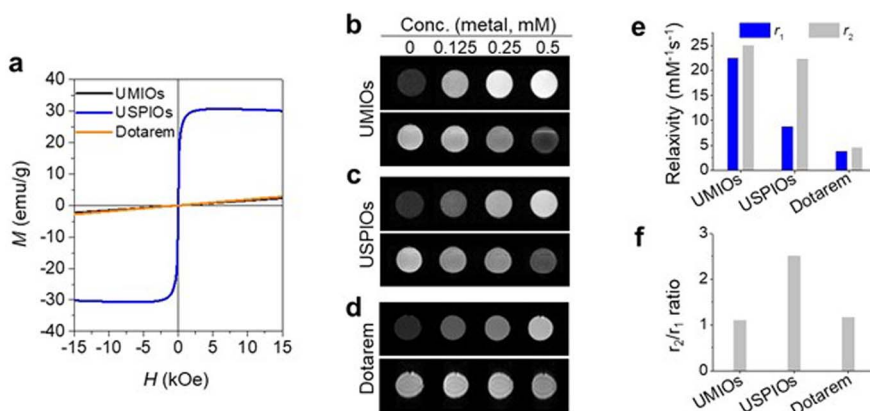

Fig. 2 Magnetic properties and T_1 magnetic resonance imaging (MRI) contrast effects of UMIOs. (a) Magnetization curves of UMIOs, USPIOs, and Dotarem. (b–d) T_1-weighted (top) and T_2-weighted (bottom) MR images of UMIOs (b), USPIOs (c), and Dotarem (d). (e) Measured r_1 and r_2 values of UMIOs, USPIOs, and Dotarem. (f) Calculated r_2/r_1 ratios of UMIOs, USPIOs, and Dotarem. MR images were obtained using a 3 T MRI scanner.
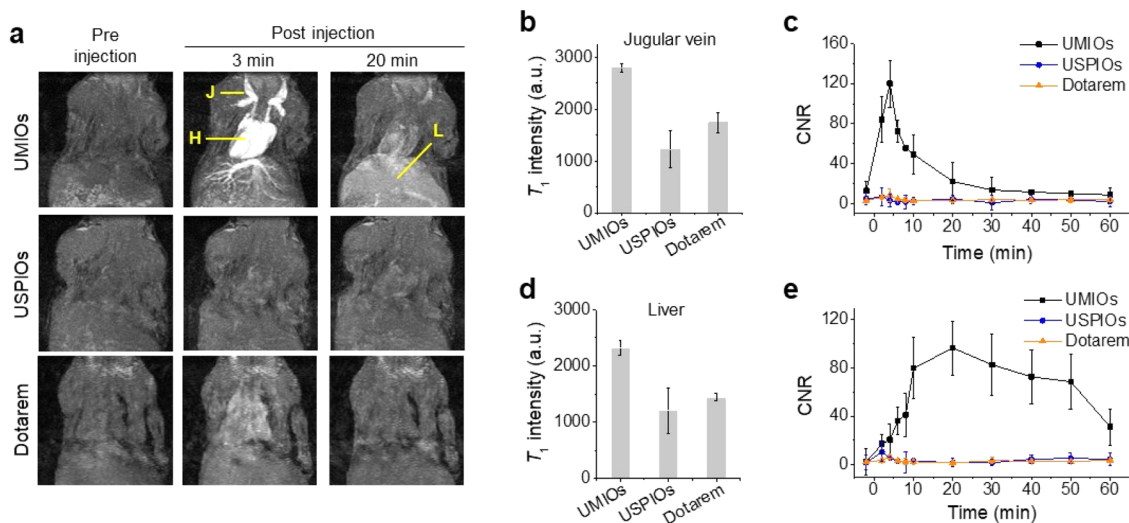
Fig. 3 Sequential MR imaging of blood vessels and the liver using UMIOs and comparison with those acquired using USPIOs and Dotarem. (a) T_1 MR images of UMIO (top), USPIO (middle), and Dotarem (bottom) injected mice at a dosage of 2.8 mg_{metal} kg^{-1}. J, H, and L represent the jugular vein, heart, and liver, respectively. (b and c) Maximum T_1 intensity (b) and time-dependent variations in the contrast-to-noise ratio (CNR, (c)) measured for the jugular vein. (d and e) Maximum T_1 intensity (d) and time-dependent changes in the CNR (e) evaluated for the liver. MR images were obtained using a 3 T MRI scanner.

For *in vivo* T_1 MR imaging, UMIOs were intravenously injected into mice at dosages of 1.4, 2.8, and 5.6 mg_{Fe+Mn} kg^{-1}. A series of MR images were obtained for 1 h using the 3 T MRI scanner [Fig. 3a (top) and S13†]. After 3 min of administration, the brightest T_1 signal was observed from the jugular vein and heart, and the hepatic vein in the liver was also clearly depicted. However, after 20 min of administration, the intensities of the signals from the jugular vein and heart decreased, whereas that of the signal from the liver substantially increased [Fig. 3a (top)]. Although these sequential blood vessel and liver contrast effects were noticed at all tested dosages, the optimal dosage was found to be 2.8 mg_{metal} kg^{-1} [~0.05 mmol kg^{-1}, Fig. 3a (top) and S13†]. In contrast, the blood vessels or liver of the mice injected with USPIOs exhibited no noticeable contrast effects [Fig. 3a (middle)]. For the Dotarem injected mouse, there was a weak contrast enhancement observed in the jugular vein and heart at the same dosage (0.05 mmol kg^{-1}), but no significant contrast enhancement was observed in the liver [Fig. 3a (bottom)]. When the T_1 intensities (Fig. 3b) and contrast-to-noise ratios (CNRs) of UMIOs (Fig. 3c) were evaluated at the jugular vein, these were significantly higher as compared to those of USPIOs and Dotarem. After 4 min of injection, the maximum CNRs for UMIOs were observed and the values were 120.1 (Fig. 3c). And then, the CNR for the jugular vein continuously decreased to the baseline (Fig. 3b and c), whereas the CNR for the liver substantially increased (Fig. 3d and e). A maximum CNR of 96.4 was observed in the liver after approximately 20 min of injection of UMIOs, whereas maximum CNRs of only 10.4 and 6.5 were noticed after ~4 min of injection of USPIOs and Dotarem (Fig. 3e). In T_2-weighted MR images obtained after 1 h of injection, no changes in signal intensity were observed in the liver for UMIOs, indicating that UMIOs were effectively cleared from the liver without accumulation

(Fig. S14†). In contrast, USPIOs exhibited strong dark contrasts in the liver under identical experimental conditions, showing their liver accumulation (Fig. S14†).

The monitoring of the T_1 signal at the liver for 24 hours (Fig. 4a and b) revealed interesting findings. Similar to the result shown in Fig. 3e, a high T_1 signal intensity in the liver was
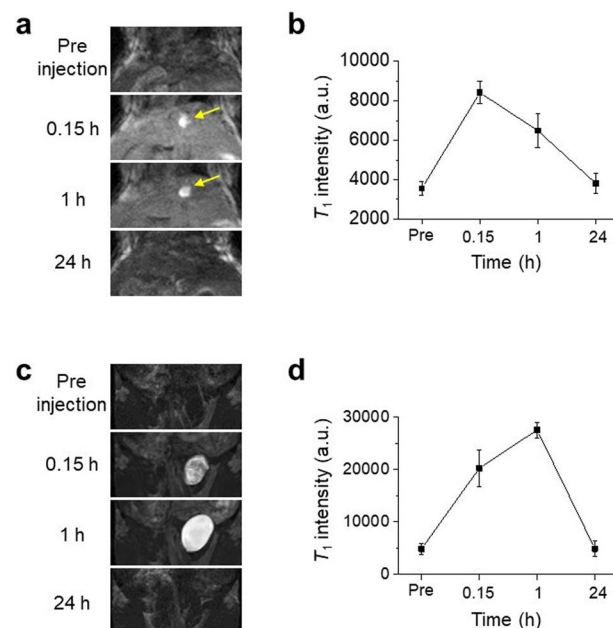

Fig. 4 Excretion characteristics of UMIOs. (a and b) T_1-weighted MR images of the liver monitored for 24 h after administration of UMIOs (a) and the measured T_1 intensity (b). (c and d) T_1-weighted MR images of the bladder monitored for 24 h after administration of UMIOs (c) and the evaluated T_1 intensity (d). MR images were obtained using a 9.4 T MRI scanner.

observed after 0.15 h of injection followed by a considerable decrease in the signal intensity after 1 h of injection of UMIOs. However, interestingly, a bright contrast (indicated by the yellow arrow in Fig. 4a) was acquired in the gallbladder after not only 0.15 h, but also 1 h of injection of UMIOs. The signals for both the liver and gallbladder completely disappeared after 24 h of injection of UMIOs (Fig. 4a). This temporary presence of UMIOs in the gallbladder provides evidence of hepatobiliary excretion, which involves the secretion of nanomaterials from hepatocytes into the bile, temporary storage/condensation of bile in the gallbladder, and excretion into small intestines and feces.[18] The presence of a dark signal in the T_2-weighted MR image acquired at 60 min after administration (yellow arrow, Fig. S14†) further supports the observation of UMIO condensation in the gallbladder. Hepatocyte uptakes of UMIOs are possibly associated with the binding of UMIOs to SLC39A14, a transmembrane metal transporter, which has recently been reported to play a vital role in maintaining Mn homeostasis in the liver.[31,32] These findings suggest that UMIOs undergo hepatobiliary clearance, which is a more favorable and faster route as compared to the monophagocytic system that often leads to long-term retention of nanoparticles in the liver.[18] The absence of aggregation or accumulation of UMIOs in the liver observed for seven days in T_2-weighted MR images also indirectly supports the hepatobiliary excretion of UMIOs (Fig. S15†). Although we observed hepatobiliary excretion of UMIOs, it is important to note that the hydrodynamic sizes of UMIOs are approximately 3 nm, which are smaller than the renal clearance limit of 5–7 nm. Therefore, UMIOs can also be excreted *via* the renal route.[65] The contrast of the bladder of UMIO injected mice significantly increased in MR images, confirming that UMIOs excreted *via* renal clearance and were collected in the bladder (Fig. 4c and d). These findings imply the excretion of UMIOs *via* both renal clearance and hepatobiliary pathways following administration.

Conclusions

We have successfully developed UMIOs and demonstrated their potential as liver specific contrast agents for T_1 MRI. UMIOs offer several advantages, including a non-gadolinium-based composition and outstanding T_1 contrast effects with ideally low r_2/r_1 values, surpassing the performances of previously reported USPIOs. These unique imaging abilities of UMIOs enable sequential imaging of blood vessels and the liver with robust T_1 signal intensities and high CNRs. Moreover, the presence of hepatobiliary excretion and potential for renal clearance, as demonstrated by MR imaging of the gallbladder and bladder, indicate the excellent biocompatibilities and safeties of UMIOs. It is important to note, however, that a comprehensive long-term study will be necessary to ascertain the safety of UMIOs conclusively. The distinctive capability of UMIOs for hepatocyte uptake, hepatobiliary excretion, and renal excretion, in contrast to conventional USPIOs or SPIOs, suggests their potential as future liver contrast agents for the safe and accurate diagnosis of liver diseases.

Author contributions

Conceptualization, data curation, funding acquisition investigation methodology, project administration, supervision, writing – original draft, and review & editing: JK, TS, and JC; formal analysis, validation, and visualization: SL, AB, JJ, JS, JY, and ML.

Conflicts of interest

There are no conflicts to declare.

Acknowledgements

References

1 B. E. Van Beers, B. Gallez and J. Pringot, *Radiology*, 1997, **203**, 297–306.

2 M. R. Oliva, *Cancer Imag.*, 2004, **4**, S42–S46.

3 B. E. Van Beers, C. M. Pastor and H. K. Hussain, *J. Hepatol.*, 2012, **57**, 421–429.

4 Y. L. Thian, A. M. Riddell and D.-M. Koh, *Cancer Imag.*, 2013, **13**, 567–579.

5 P. Reimer, G. Schneider and W. Schima, *Eur. Radiol.*, 2004, **14**, 559–578.

6 M. Leonhardt, M. Keiser, S. Oswald, J. Kühn, J. Jia, M. Grube, H. K. Kroemer, W. Siegmund and W. Weitschies, *Drug Metab. Dispos.*, 2010, **38**, 1024–1028.

7 H.-J. Weinmann, H. Bauer, T. Frenzel, A. Mühler and W. Ebert, *Acad. Radiol.*, 1996, **3**, S232–S234.

8 G. Zollner, M. Wagner, P. Fickert, D. Silbert, A. Fuchsbichler, K. Zatloukal, H. Denk and M. Trauner, *Liver Int.*, 2005, **25**, 367–379.

9 P. Marckmann, L. Skov, K. Rossen, A. Dupont, M. B. Damholt, J. G. Heaf and H. S. Thomsen, *J. Am. Soc. Nephrol.*, 2006, **17**, 2359–2362.

10 T. Grobner, *Nephrol., Dial., Transplant.*, 2006, **21**, 1104–1108.

11 M. S. Davenport, B. L. Viglianti, M. M. Al-Hawary, E. M. Caoili, R. K. Kaza, P. S. C. Liu, K. E. Maturen, T. L. Chenevert and H. K. Hussain, *Radiology*, 2013, **266**, 452–461.

12 U. Motosugi, P. Bannas, C. A. Bookwalter, K. Sano and S. B. Reeder, *Radiology*, 2016, **279**, 93–102.

13 Y. Cao, Z. Mao, Y. He, Y. Kuang, M. Liu, Y. Zhou, Y. Zhang and R. Pei, *ACS Appl. Mater. Interfaces*, 2020, **12**, 26973–26981.

14 Z. Shen, A. Wu and X. Chen, *Mol. Pharm.*, 2017, **14**, 1352–1364.

15 H. Arami, A. Khandhar, D. Liggitt and K. M. Krishnan, *Chem. Soc. Rev.*, 2015, **44**, 8576–8607.

16 J. H. Lim, D. Choi, S. K. Cho, S. H. Kim, W. J. Lee, H. K. Lim, C. K. Park, S. W. Paik and Y. I. Kim, *Radiology*, 2001, **220**, 669–676.

17 W. Ngo, S. Ahmed, C. Blackadar, B. Bussin, Q. Ji, S. M. Mladjenovic, Z. Sepahi and W. C. W. Chan, *Adv. Drug Delivery Rev.*, 2022, **152**, 114238.

18 D. Wilson and M. A. Langell, *Appl. Surf. Sci.*, 2014, **303**, 6–13.

19 H. Wei, O. T. Bruns, M. G. Kaul, E. C. Hansen, M. Barch, A. Wiśniowska, O. Chen, Y. Chen, N. Li, S. Okada, J. M. Cordero, M. Heine, C. T. Farrar, D. M. Montana, G. Adam, H. Ittrich, A. Jasanoff, P. Nielsen and M. G. Bawendi, *Proc. Natl. Acad. Sci. U. S. A.*, 2017, **114**, 2325–2330.

20 A. Kostopoulou, I. Tsiaoussis and A. Lappas, *Photon. Nanostruct: Fundam. Appl.*, 2011, **9**, 201–206.

21 I. Fernández-Barahona, M. Muñoz-Hernando, J. Ruiz-Cabello, F. Herranz and J. Pellico, *Inorganics*, 2020, **8**, 28.

22 B. H. Kim, N. Lee, H. Kim, K. An, Y. I. Park, Y. Choi, K. Shin, Y. Lee, S. G. Kwon, H. B. Na, J.-G. Park, T.-Y. Ahn, Y.-W. Kim, W. K. Moon, S. H. Choi and T. Hyeon, *J. Am. Chem. Soc.*, 2011, **133**, 12624–12631.

23 Z. Shen, T. Chen, X. Ma, W. Ren, Z. Zhou, G. Zhu, A. Zhang, Y. Liu, J. Song, Z. Li, H. Ruan, W. Fan, L. Lin, J. Munasinghe, X. Chen and A. Wu, *ACS Nano*, 2017, **11**, 10992–11004.

24 G. Wang, X. Zhang, A. Skallberg, Y. Liu, Z. Hu, X. Mei and K. Uvdal, *Nanoscale*, 2014, **6**, 2953–2963.

25 L. Zeng, W. Ren, J. Zheng, P. Cui and A. Wu, *Phys. Chem. Chem. Phys.*, 2012, **14**, 2631–2636.

26 N. Nimi, A. Saraswathy, S. S. Nazeer, N. Francis, S. J. Shenoy and R. S. Jayasree, *Biomaterials*, 2018, **171**, 46–56.

27 L. Wang, J. Huang, H. Chen, H. Wu, Y. Xu, Y. Li, H. Yi, Y. A. Wang, L. Yang and H. Mao, *ACS Nano*, 2017, **11**, 4582–4592.

28 Z. Liu, J. Cai, H. Su, J. Yang, W. Sun, Y. Ma, S. Liu and C. Zhang, *RSC Adv.*, 2017, **7**, 31671–31681.

29 R. H. Hashemi, W. G. Bradley and C. J. Lisanti, *MRI: The Basics*, Lippincott Williams & Wilkins, New York, 2nd edn, 2004.

30 F. H. L. Starsich, C. Eberhardt, K. Keevend, A. Boss, A. M. Hirt, I. K. Herrmann and S. E. Pratsinis, *ACS Appl. Bio Mater.*, 2018, **1**, 783–791.

31 K. Tuschl, E. Meyer, L. E. Valdivia, N. Zhao, C. Dadswell, A. Abdul-Sada, C. Y. Hung, M. A. Simpson, W. K. Chong, T. S. Jacques, R. L. Woltjer, S. Eaton, A. Gregory, L. Sanford, E. Kara, H. Houlden, S. M. Cuno, H. Prokisch, L. Valletta, V. Tiranti, R. Younis, E. R. Maher, J. Spencer, A. Straatman-Iwanowska, P. Gissen, L. A. M. Selim, G. Pintos-Morell, W. Coroleu-Lletget, S. S. Mohammad, S. Yoganathan, R. C. Dale, M. Thomas, J. Rihel, O. A. Bodamer, C. A. Enns, S. J. Hayflick, P. T. Clayton, P. B. Mills, M. A. Kurian and S. W. Wilson, *Nat. Commun.*, 2016, **7**, 11601.

32 Y. Xin, H. Gao, J. Wang, Y. Qiang, M. U. Imam, Y. Li, J. Wang, R. Zhang, H. Zhang, Y. Yu, H. Wang, H. Luo, C. Shi, Y. Xu, S. Hojyo, T. Fukada, J. Min and F. Wang, *Cell Discovery*, 2017, **3**, 1–13.

33 X. Lu, H. Zhou, Z. Liang, J. Feng, Y. Lu, L. Huang, X. Qiu, Y. Xu and Z. Shen, *J. Nanobiotechnol.*, 2022, **20**, 1–11.

34 H. Nosrati, M. Salehiabar, M. Fridoni, M.-A. Abdollahifar, H. Kheiri Manjili, S. Davaran and H. Danafar, *Sci. Rep.*, 2019, **9**, 7173.

35 R. Weissleder, D. Stark, B. Engelstad, B. Bacon, C. Compton, D. White, P. Jacobs and J. Lewis, *Am. J. Roentgenol.*, 1989, **152**, 167–173.

36 Z. Li, B. Tan, M. Allix, A. I. Cooper and M. J. Rosseinsky, *Small*, 2008, **4**, 231–239.

37 Z. Li, P. W. Yi, Q. Sun, H. Lei, H. Li Zhao, Z. H. Zhu, S. C. Smith, M. B. Lan and G. Q. M. Lu, *Adv. Funct. Mater.*, 2012, **22**, 2387–2393.

38 A. K. Hauser, R. Mathias, K. W. Anderson and J. Z. Hilt, *Mater. Chem. Phys.*, 2015, **160**, 177–186.

39 B. Chen, Z. Guo, C. Guo, Y. Mao, Z. Qin, D. Ye, F. Zang, Z. Lou, Z. Zhang, M. Li, Y. Liu, M. Ji, J. Sun and N. Gu, *Nanoscale*, 2020, **12**, 5521–5532.

40 S. Arsalani, Y. Hadadian, E. E. Mazon, E. J. Guidelli, E. Kava, A. P. Ramos, A. J. Gualdi, T. Z. Pavan, O. Baffa and A. A. O. Carneiro, *J. Magn. Magn. Mater.*, 2022, **564**, 170091.

41 G. Wang, X. Zhang, A. Skallberg, Y. Liu, Z. Hu, X. Mei and K. Uvdal, *Nanoscale*, 2014, **6**, 2953–2963.

42 I. Reyes-Molina, A. Hernández-Rodríguez, C. Cabal-Mirabal and E. Gonzalez-Dalmau, *Res. Sq.*, 2022, **1**, 1–18.

43 J. R. Shin, G. S. An and S.-C. Choi, *Processes*, 2021, **9**, 1795.

44 S. Algessair, O. M. Lemine, N. Madkhali and K. El-Boubbou, *Appl. Phys. A*, 2023, **129**, 814.

45 L. Gao, Z. Liu, Z. Yang, L. Cao, C. Feng, M. Chu and J. Tang, *Appl. Surf. Sci.*, 2020, **508**, 145292.

46 E. S. Ilton, J. E. Post, P. J. Heaney, F. T. Ling and S. N. Kerisit, *Appl. Surf. Sci.*, 2016, **366**, 475–485.

47 J. Guo, H. Zhang, Z. He, S. Li and Z. Li, *J. Mater. Sci.: Mater. Electron.*, 2017, **29**, 2491–2499.

48 N. Li, F. Fu, J. Lu, Z. Ding, B. Tang and J. Pang, *Environ. Pollut.*, 2017, **220**, 1376–1385.

49 Y. Ma, X. Xu, L. Lu, K. Meng, Y. Wu, J. Chen, J. Miao and Y. Jiang, *Ceram. Int.*, 2021, **47**, 34005–34011.

50 C. Koo, H. Hong, P. W. Im, H. Kim, C. Lee, X. Jin, B. Yan, W. Lee, H.-J. Im, S. H. Paek and Y. Piao, *Nano Convergence*, 2020, **7**, 1–9.

51 H. Kohzadi and M. Soleiman-Beigi, *Sci. Rep.*, 2021, **11**, 24508.

52 Q. Sun, L. Sun, Y. Cai, T. Ji and G. Zhang, *RSC Adv.*, 2018, **8**, 35337–35342.

53 Y.-N. Zhang, W. Poon, A. J. Tavares, I. D. McGilvray and W. C. W. Chan, *J. Controlled Release*, 2016, **240**, 332–348.

54 D. Wilson and M. A. Langell, *Appl. Surf. Sci.*, 2014, **303**, 6–13.

55 I. Crăciunescu, P. Palade, N. Iacob, G. M. Ispas, A. E. Stanciu, V. Kuncser and R. P. Turcu, *J. Phys. Chem. C*, 2021, **125**, 11132–11146.

56 J. Ma, B. Zhao, H. Xiang, F.-Z. Dai, Y. Liu, R. Zhang and Y. Zhou, *J. Adv. Ceram.*, 2022, **11**, 754–768.

57 L. Zhang, X. Zhao, C. Niu, N. Tang, H. Guo, X. Wen, C. Liang and G. Zeng, *Chem. Eng. J.*, 2019, **362**, 851–864.

58 X. Li, Y. Huang, H. Liu, C. Wu, W. Bi, Y. Yuan and X. Liu, *J. Environ. Sci.*, 2018, **64**, 42–50.

59 B. Rincón-Tomás, B. Khonsari, D. Mühlen, C. Wickbold, N. Schäfer, D. Hause-Reitner, M. Hoppert and J. Reitner, *Int. J. Astrobiol.*, 2016, **15**, 219–229.

60 Y. Luo, J. Ding, Y. Shen, W. Tan, G. Qiu and F. Liu, *Chem. Geol.*, 2018, **488**, 162–170.

61 D. Sibera, U. Narkiewicz, N. Guskos and G. Zołnierkiewicz, *J. Phys.: Conf. Ser.*, 2009, **146**, 012014.

62 G. S. Shahane, K. V. Zipare and R. P. Pant, *Magnetohydrodynamics*, 2013, **49**, 317–321.

63 S. I. Andronenko and S. K. Misra, *Appl. Magn. Reson.*, 2015, **46**, 693–707.

64 Z. Zhao, C. Sun, J. Bao, L. Yang, R. Wei, J. Cheng, H. Lin and J. Gao, *J. Mater. Chem. B*, 2018, **6**, 401–413.

65 H. S. Choi, W. Liu, P. Misra, E. Tanaka, J. P. Zimmer, B. I. Ipe, M. G. Bawendi and J. V. Frangioni, *Nat. Biotechnol.*, 2007, **25**, 1165–1170.